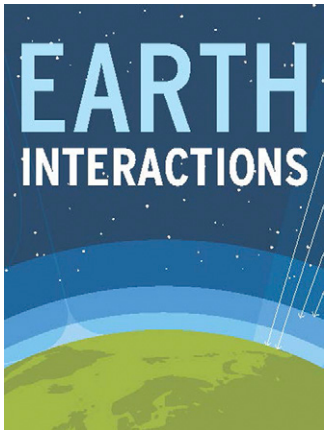

Improvements in Land-Use Classification for Estimating Daytime Surface Temperatures and Sea-Breeze Flows in Southern California

Pedro Sequera[a] and Jorge E. González[a]

Department of Mechanical Engineering, City College of New York, City University of New York, New York, New York

Kyle McDonald

Department of Earth and Atmospheric Sciences, City College of New York, City University of New York, New York, New York

Steve LaDochy

Department of Geosciences and Environment, California State University, Los Angeles, Los Angeles, California

Daniel Comarazamy

NOAA-CREST Center, City College of New York, City University of New York, New York, New York

Received 10 October 2014; in final form 4 March 2016

[a] Corresponding author address: Jorge E. González, Department of Mechanical Engineering, The City College of New York, 140th street and Convent Avenue, Steinman Hall, Room T-238, New York, NY 10031.

E-mail address: gonzalez@me.ccny.cuny.edu

DOI: 10.1175/EI-D-14-0034.1

ABSTRACT: Understanding the interactions between large-scale atmospheric and oceanic circulation patterns and changes in land cover and land use (LCLU) due to urbanization is a relevant subject in many coastal climates. Recent studies by Lebassi et al. found that the average maximum air temperatures during the summer in two populated California coastal areas decreased at low-elevation areas open to marine air penetration during the period of 1970–2005. This coastal cooling was attributed to an increase in sea-breeze activity.

The aims of this work are to better understand the coastal flow patterns and sea–land thermal gradient by improving the land-cover classification scheme in the region using updated airborne remote sensing data and to assess the suitability of the updated regional atmospheric modeling system for representing maritime flows in this region. This study uses high-resolution airborne data from the NASA Hyperspectral Infrared Imager (HyspIRI) mission preparatory flight campaign over Southern California and surface ground stations to compare observations against model estimations.

Five new urban land classes were created using broadband albedo derived from the Airborne Visible and Infrared Imaging Spectrometer (AVIRIS) sensor and then assimilated into the Weather Research and Forecasting (WRF) Model. The updated model captures the diurnal spatial and temporal sea-breeze patterns in the region. Results show notable improvements of simulated daytime surface temperature and coastal winds using the HyspIRI-derived products in the model against the default land classification, reaffirming the importance of accounting for heterogeneity of urban surface properties.

KEYWORDS: Circulation/dynamics; Atmosphere–land interaction; Atmosphere/ocean structure/phenomena; Sea breezes; Observational techniques and algorithms; Remote sensing; Mathematical and statistical techniques; Classification; Models and modeling; Mesoscale models; Applications; Land use

1. Introduction

It is well known that human-induced landscape changes have many impacts on local and regional-scale climate. Changes due to urbanization directly impact the nature of the surface and atmospheric properties of a region by altering the natural energy and hydrologic balances (Oke 1984; Schmid and Oke 1992). The most documented effect linked to urbanization is the urban heat island (UHI), in which the air above the urban canopy is usually warmer than the air in the rural surroundings as a consequence of urban/rural thermal energy budget differences (Oke 1982). The magnitude and characteristics of the UHI are controlled by several factors. In general, UHI decreases with increasing wind speed and cloud cover, while it increases with city size and population density; it is also stronger during summer and, typically, the nighttime, depending on location (Arnfield 2003).

Even though the general UHI pattern is similar in all urban environments, each city is exposed to diverse local and synoptic factors, especially at midlatitude coastal cities where the effects of the UHI on regional influences merge with large-scale atmospheric and oceanic circulation patterns. Several studies have documented and modeled the effects of the UHI in regional temperatures and mesoscale flow patterns (Yoshikado 1992, 1994; Kitada et al. 1998; Kusaka et al. 2000; Ohashi and Kida 2002; Lo et al. 2007; Shepherd et al. 2010; Dandou et al. 2009; Carter et al. 2012). Overall, these studies conclude that large cities contribute to an enhanced coastal temperature gradient, resulting in thermal mesoscale circulations

where the UHI and sea-breeze front converge. Moreover, if an inland urban area exists, the combined urban–coastal circulation is stronger and lasts longer than a typical sea breeze (Ohashi and Kida 2002).

California is a good example of a coastal region that has undergone intense urbanization. In 1900, California was home to less than 2 million people; by 1950, the population had reached 10 million. California's population nearly tripled in the last half of the twentieth century, reaching up to 37 million in 2010, out of which, approximately 70% live in coastal regions (U.S. Census Bureau 2010).

Many studies have confirmed that average California air temperatures at 2-m above ground level (AGL) increased over the past four decades. During the summer in particular, these trends show diurnal asymmetric warming rates: in coastal areas, nighttime minimum temperatures $T_{\min}$ have warmed faster than daytime maximum values $T_{\max}$, thus decreasing the diurnal temperature range. The observed asymmetric warming at California coastal sites has been variously attributed to changes in cloud cover (Nemani et al. 2001), sea surface temperatures (SSTs; Karl et al. 1993), upwelling (Bakun 1990; Snyder et al. 2003; McGregor et al. 2007), changes in land cover/land use (LCLU; Mintz 1984; Zhang 1997; Chase et al. 2000; Pielke et al. 2002), irrigation (Christy et al. 2006; Bonfils and Lobell 2007), greenhouse gases (GHGs; Duffy et al. 2007; Walters et al. 2007; Cayan et al. 2008; Cordero et al. 2011), Pacific decadal oscillation (PDO; Douville 2003; LaDochy et al. 2004, 2007; Clark 2010), and/or UHI (LaDochy et al. 2007; Dai et al. 1999; Kalnay and Cai 2003; Diem et al. 2006). In particular, LaDochy et al. (2007) observed warming rates in large urban sites over twice as high as those for the state for annual average minimum $T_{\min}$ and maximum temperatures $T_{\max}$ from 1950 to 2000, in agreement with the expected UHI effects.

The regional warming pattern, however, changes in the summer, as low-elevation coastal urban areas [Southern California air basin (SoCAB) and San Francisco Bay Area (SFBA)] have cooling $T_{\max}$ trends from 1970 to 2005, while both inland and higher-elevation coastal regions are warming (Lebassi et al. 2009). These observations, along with mesoscale modeling results (Lebassi-Habtezion et al. 2011), led the authors (Lebassi et al. 2009; Lebassi-Habtezion et al. 2011) to hypothesize that the coastal cooling effect was the consequence (and a ''reverse reaction'') of GHG warming in inland areas, which resulted in increased sea-breeze flow activity. This hypothesis is also supported by an observed increase in the sea–land pressure gradient of 0.04 hPa 100 km^{-1} decade^{-1} over the last three decades in the region (Lebassi et al. 2009). Further studies have detected additional coastal cooling of air basins in San Diego, San Luis Obispo (P. Sequera et al. 2016, unpublished manuscript), and the central coast (Potter 2014). These findings raise the question regarding which are the factors that drive this phenomenon since the cooling needs to overcome both GHG and UHI [not accounted for in Lebassi-Habtezion et al. (2011)] warming influences.

Previous modeling efforts have studied the impacts of surface characteristic modifications on Southern California's local climate. Numerical simulations performed on the Los Angeles basin by Sailor (1995) indicated that increasing albedo over downtown Los Angeles by 0.14 and over the entire basin by an average of 0.08 would result in decreased peak summertime temperatures by as much as 1.5°C, lowering boundary layer heights by more than 50 m and reducing the magnitude and penetration of the sea breeze. One-dimensional meteorological simulations by

Taha et al. (1988) showed that localized afternoon air temperatures on summer days can be lowered by as much as 4°C by changing the surface albedo from 0.25 to 0.40 in a typical, midlatitude warm climate. Three-dimensional mesoscale simulations of the effects of large-scale albedo increases in the Los Angeles basin showed similar magnitudes of impacts on air temperature in summer; an average decrease of 2°C and up to 4°C may be possible by increasing the albedo by 0.13 in urbanized areas of the basin (Taha 1994). While these studies focused on analyzing the impact of urban surface characteristic modifications on the local climate, they do not account for high-resolution urban surface parameters that can significantly alter the regional circulations (Carter et al. 2012).

To understand the impacts of urbanization on surface temperatures and daily sea-breeze patterns in the region, an adequate representation of the urban landscape and heterogeneity must be provided. This is an important issue to address in climate modeling studies given that most land-cover classification schemes assign a unique set of surface properties to the urban land class. The aim of this work is therefore to improve the land-cover classification scheme in Southern California using updated high-resolution airborne remote sensing data from the recent HyspIRI Mission Preparatory Flight campaigns and to assess the suitability of the updated regional atmospheric modeling system to represent T_{max} and sea breeze. The new urban land classes are here derived through a classification algorithm on the surface broadband albedo. Even though the surface energy balance in urban areas depends on other parameters such as emissivity, surface roughness, and vegetation fraction, the use of albedo to create the new land classes is justified since daily maximum temperatures, and therefore sea breezes, are most influenced by this parameter (Giridharan et al. 2004; Krayenhoff and Voogt 2010; Comarazamy et al. 2010). Krayenhoff and Voogt (2010) studied the sensitivity of near-surface air temperatures to changes in roof albedo in neighborhoods with different degrees of urbanization in Basel and Chicago, concluding that the temperature sensitivity to albedo is significantly higher (over 65%) during summer and at daytime when comparing to other seasons because of higher solar elevation angles. A UHI study conducted by Giridharan et al. (2004) in Hong Kong during summer also showed that near-surface temperatures were most sensitive to surface albedo, sky view factor, and total height to floor area ratio over other surface properties. Similar results were reported by Comarazamy et al. (2010) in San Juan, Puerto Rico, where updated land classes using albedo as the parameter for classification lead to improvements on the estimation of daily maximum temperatures. While most studies have focused on the sensitivity of near-surface temperatures to albedo, very few have examined the impacts of albedo on sea-breeze patterns. Carter et al. (2012) showed that while coastal morphology can itself lead to complex sea-breeze front structures, including preferred areas of vertical motion, the urban environment also has a large impact on the evolution of the sea-breeze mesoscale boundary. Their work also showed that even reduced resolution urban canopy parameters, such as the increased mechanical turbulence from tall buildings, the albedo of paved surfaces, and the urban canyon effect, can alter the simulation of complex circulations in the region.

This study is a major step toward understanding the combined effects of large-scale (GHG and PDO) and regional-scale (UHI) factors on summer coastal cooling following the methodology developed by Comarazamy et al. (2010, 2013). This

approach integrates ground and remote sensing information (Comarazamy et al. 2010) as well as mesoscale atmospheric modeling and statistical techniques (Comarazamy et al. 2013), allowing quantification of the individual and combined contributions of LCLU changes and large-scale forcings to the magnitude of observed climate change.

This paper provides a detailed description of the derivation of new land covers using recently acquired remote sensing data (section 3.1) and an assessment of the impact of the new land classes on atmospheric model estimations (sections 3.2–3.4).

2. Data and methodology

2.1. HyspIRI flight campaign and sensors

The description and updating of the urban surface characteristics in the SoCAB were performed using data from two high-resolution sensors: the Airborne Visible and Infrared Imaging Spectrometer (AVIRIS) and the MODIS/ASTER Airborne Simulator (MASTER). These two sensors were flown over Southern California on a NASA ER-2 aircraft as part of the Hyperspectral Infrared Imager (HyspIRI) mission preparatory flight campaign on 24 September 2013.

The AVIRIS is an optical sensor that delivers calibrated images of the upwelling spectral radiance in 224 contiguous spectral bands with wavelengths from 400 to 2500 nm, covering the visible and near-infrared portion of the electromagnetic (EM) spectrum (Figure 1, left). For this specific flight, the horizontal resolution was 15 m.

The MASTER sensor is an imager sensor developed for the MODIS and ASTER projects (Hook et al. 2001). The instrument has 50 channels ranging from 0.4 to 13 μm, covering the visible to the thermal infrared portion of the EM spectrum (Figure 1, right) with a horizontal resolution of 35 m.

2.2. Data processing

The original AVIRIS and MASTER level-1b calibrated radiance data underwent atmospheric correction to retrieve level-2 products: land surface reflectance, in the case of AVIRIS, and land surface emissivity and land surface temperature (LST) for MASTER. Each sensor had a different approach for atmospheric corrections and data retrieval.

An updated version of the atmospheric removal (ATREM) code (Gao and Davis 1997) for the correction of atmospheric gas absorption and molecular and aerosol scattering effects was used to retrieve land surface reflectances from AVIRIS data. This version of the ATREM code allows the retrieval of surface reflectance from imaging spectrometers without the need for field measurements of reflectance spectra. First, the transmission spectra of carbon dioxide (CO_2), ozone (O_3), nitrous oxide (N_2O), carbon monoxide (CO), methane (CH_4), and oxygen (O_2) are simulated based on the solar and observational geometry and through a channel ratio technique (Gao et al. 1993) for water vapor (H_2O). Then, the scattering effect due to atmospheric molecules and aerosols is modeled with the Second Simulation of the Satellite Signal in the Solar Spectrum (6S) computer code (Vermote et al. 1994). The measured radiances are divided by solar irradiances above the atmosphere to obtain

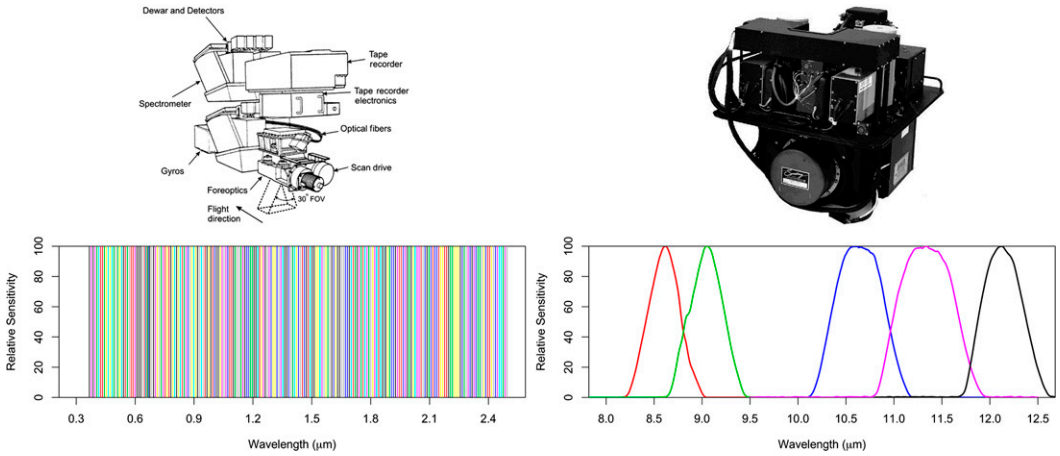

Figure 1. (left) AVIRIS and (right) MASTER spectral response curves.

apparent reflectances, and finally the surface reflectances are derived from the apparent reflectances using the simulated atmospheric gaseous transmittances and the simulated molecular and aerosol scattering data. For additional information regarding the AVIRIS atmospheric corrections, we refer the reader to Gao and Green (2010). From the level-2 AVIRIS land surface reflectance, the broadband albedo for each pixel was calculated as a weighted average for every spectral band of wavelength λ with the sky irradiance [Equation (1)]. The broadband albedo is the variable used to classify the variability of the urban landscape in the region of interest:

$$\alpha = \frac{\int_{\lambda=380\text{nm}}^{\lambda=2500\text{nm}} R_\lambda I_\lambda \, d\lambda}{\int_{\lambda=380\text{nm}}^{\lambda=2500\text{nm}} I_\lambda \, d\lambda}. \tag{1}$$

Equation (1) is the definition of broadband albedo α, where R is the surface reflectance and I is the irradiance for every wavelength band λ.

Surface emissivity and temperature were collected with the MASTER sensor, flying on the same aircraft as AVIRIS. Both quantities were determined through the temperature emissivity separation (TES; Gillespie et al. 1998) algorithm. Inputs to TES include surface radiance, which is determined from atmospherically correcting the at-sensor radiance for path radiance and atmospheric absorption and the sky irradiance through the moderate resolution atmospheric transmission (MODTRAN 3.5) radiative transfer model (Berk et al. 2005). Additional details on MASTER's atmospheric corrections can be found in Hook et al. (2001).

TES is a hybridization of two algorithms: the normalized emissivity method (NEM) and the alpha residual method. First, emissivities and temperatures are estimated with the NEM method using an iterative approach to remove downwelling sky irradiance. Next, the NEM emissivities are normalized. An empirical

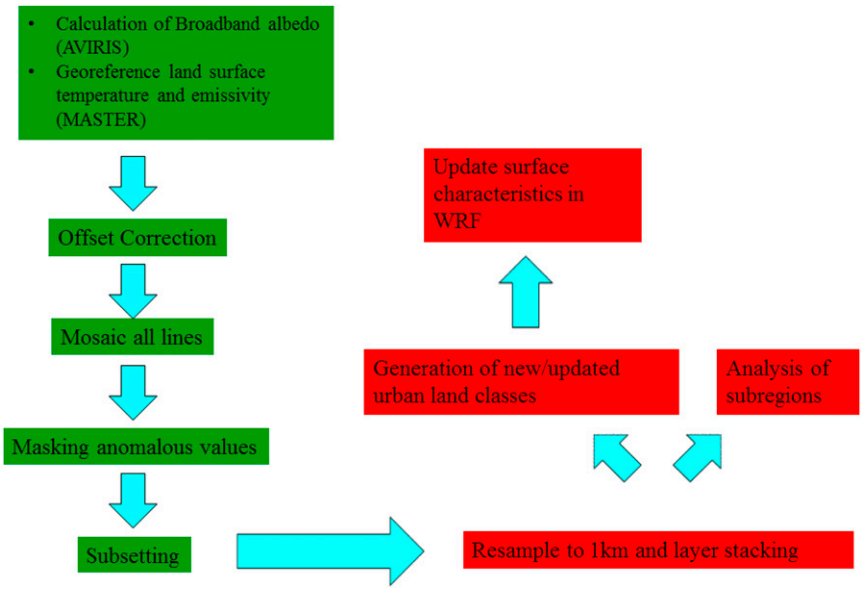

Figure 2. Overall data processing flow.

relationship based on the alpha residual method is then used to estimate the minimum emissivity, given the spectral contrast, or minimum–maximum differences (MMD), by using a calibration curve determined from laboratory measurements. TES has been shown to accurately recover temperatures within 1.5 K and emissivities within 0.015 for a wide range of surfaces and is a well-established physical algorithm (Hulley and Hook 2011).

Additional processing was performed to the broadband albedo and LST lines. The overall process (Figure 2) included offset correction for each line, removal of anomalous values, construction of a mosaic using all 10 flight lines, and subsetting the entire flight path to include only the SoCAB. Final SoCAB broadband albedo maps at 15-m resolution and LST at 35-m resolution are shown in Figure 3.

2.3. Urban characteristics update

First, the broadband albedo and LST data derived in the previous section were resampled from their original resolution to a 1 km × 1 km grid, which matches the horizontal resolution of the modeling grid. Next, the pixels corresponding to the urban and built-up class from the original MODIS IGBP land cover (Figure 4) were selected to perform the update and analysis of the regional urban extension.

New urban subclasses result from this process by use of the Clustering for Large Applications (CLARA) algorithm on the broadband albedos. The CLARA algorithm extends the *k*-medoids approach for a large number of objects by clustering a sample from the dataset and then assigning all objects in the dataset to these clusters. The *k*-medoids approach is a partitioning algorithm that clusters a dataset

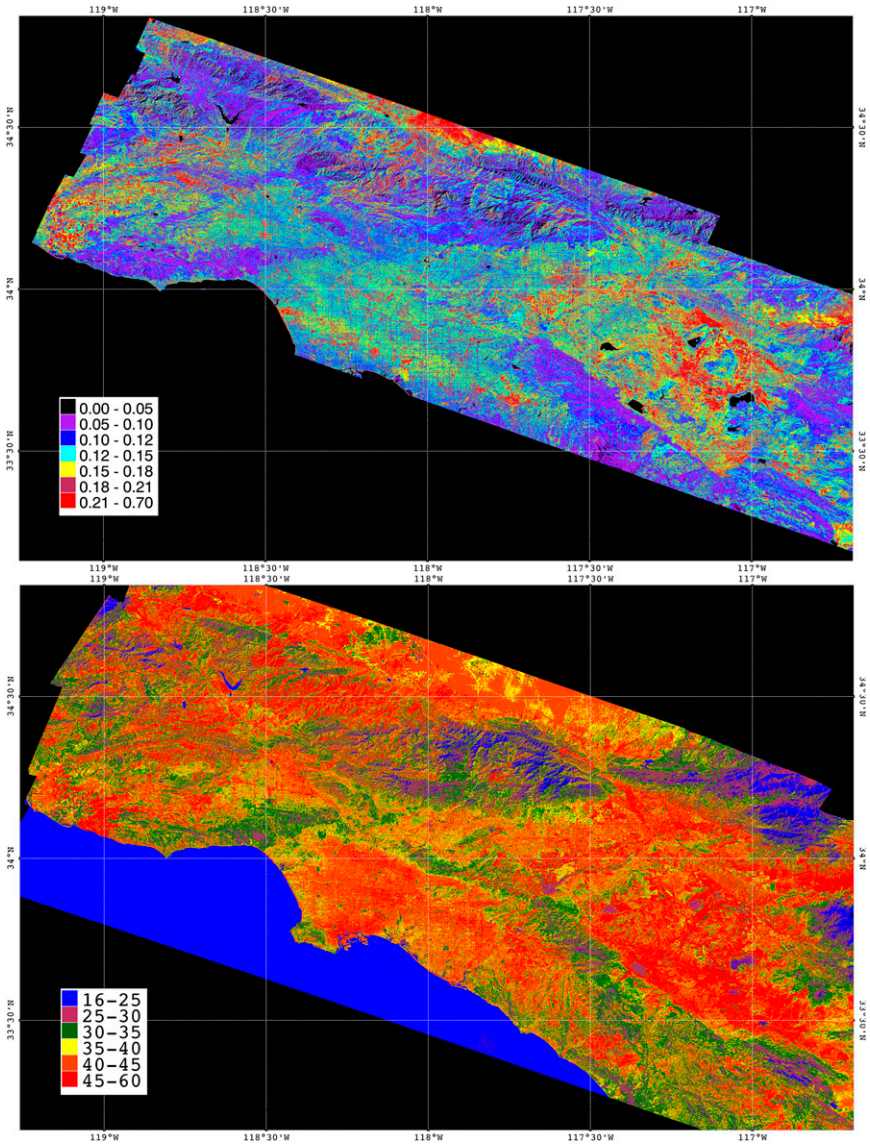

Figure 3. Products derived from the HyspIRI preparatory flight campaign over the Southern California box: (top) broadband albedo from AVIRIS at 15-m resolution and (bottom) LST (°C) from MASTER at 35-m resolution.

of n objects into k clusters known a priori by choosing a data point (or medoid) for each cluster at each iteration. Medoids for each cluster are calculated by finding a point within each cluster that minimizes the distance between itself and the other points of that cluster (Kaufman and Rousseeuw 1990).

The optimum number of subclasses was selected by using the average silhouette criterion (Rousseeuw 1987). The silhouette width is a measure of dissimilarity between one point and all other points of the same cluster. Observations with a large silhouette (almost 1) are very well clustered, whereas a small silhouette

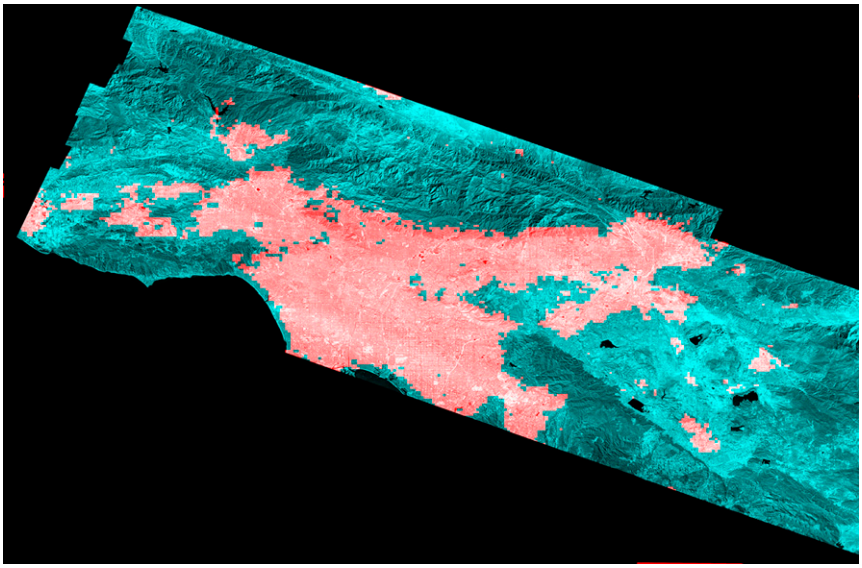

Figure 4. MODIS IGBP land-cover classification. Urban classes are shown in red and nonurban classes are shown in green.

(around 0) means that the observation lies between two clusters, and observations with a negative silhouette are probably in the wrong cluster. Hence, the optimum number of new urban classes is the one with the highest average silhouette.

2.4. Model configuration

The model chosen for this numerical experiment was the Weather Research and Forecasting (WRF, version 3.5) Model, a next-generation mesoscale numerical weather prediction system designed for both atmospheric research and operational applications (Skamarock et al. 2008).

The simulations were conducted with three horizontal nested grids with grid spacing of 16, 4, and 1 km, respectively (Figure 5). The coarser-resolution grid covers a good portion of the northern Pacific and western United States, and the finer-resolution grid covers the entire extent of the SoCAB. The vertical grid included 50 levels from 1000 to 100 hPa, covering up to an altitude of approximately 16.12 km. Boundary conditions were provided every 6 h by the National Centers for Environmental Prediction (NCEP) 2.5° reanalysis data (Kalnay et al. 1996) for all simulations, in addition to the 1° resolution NOAA's Optimum Interpolation Sea Surface Temperature analysis (Reynolds 1988) for initial conditions of SSTs. NCEP reanalysis was chosen over other higher-resolution datasets (e.g., NARR or NAM), since future modeling studies will be performed as far back as the 1950s and NCEP is the only available dataset for that timeframe.

The Mellor–Yamada–Nakanishi–Niino (MYNN) level 2.5 (Nakanishi and Niino 2004), a turbulent kinetic energy (TKE)–based local mixing scheme, was used as the planetary boundary layer (PBL) scheme. The land surface for all domains was

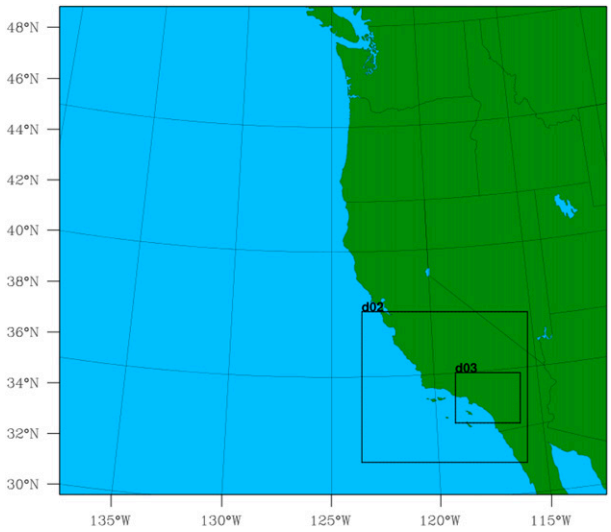

Figure 5. Model grids used in the numerical simulations.

characterized by means of the Noah land surface model (Noah LSM). Noah LSM uses four soil layers (for temperature, water + ice, and water), one vegetation type in each grid cell without dynamic vegetation and carbon budget (Jin et al. 2010), and predicts soil moisture and temperature in four layers. The ground heat budget in the Noah LSM is calculated using a diffusion equation for soil temperature, and the surface skin temperature is determined using a single, linearized surface energy balance equation (Chen and Dudhia 2001). The radiation parameterization in this scheme includes the Rapid Radiative Transfer Model (RRTM) for longwave atmospheric radiation (Skamarock et al. 2008) and the Dudhia scheme (Dudhia 1989) for shortwave atmospheric radiation.

Two different LCLU scenarios were configured for the validation in order to assess the sensitivity of surface temperature and wind speed to different surface characteristics. The first scenario (Figure 6, top) is the MODIS land-cover classification of the International Geosphere–Biosphere Programme (MODIS IGBP), which includes 20 categories of land use (Friedl et al. 2010). The second LCLU scenario (Figure 6, bottom) is the same MODIS IGBP with additional subcategories for the urban and built-up classes derived from the hyperspectral sensor data, as explained in section 2.3.

2.5. Ground observational data

The WRF outputs for 2-m AGL (above ground level) temperatures and 10-m AGL wind speeds were compared against hourly observations from 18 meteorological terminal aviation routine (METAR) ground stations in the SoCAB (Figure 7) by using the model grid point closest to each observational site. Both WRF outputs for these variables, and observations, are hereafter referred to as "surface" values. WRF skin temperature at the time of the flight was also compared to MASTER-derived LSTs to compare model outputs with airborne data.

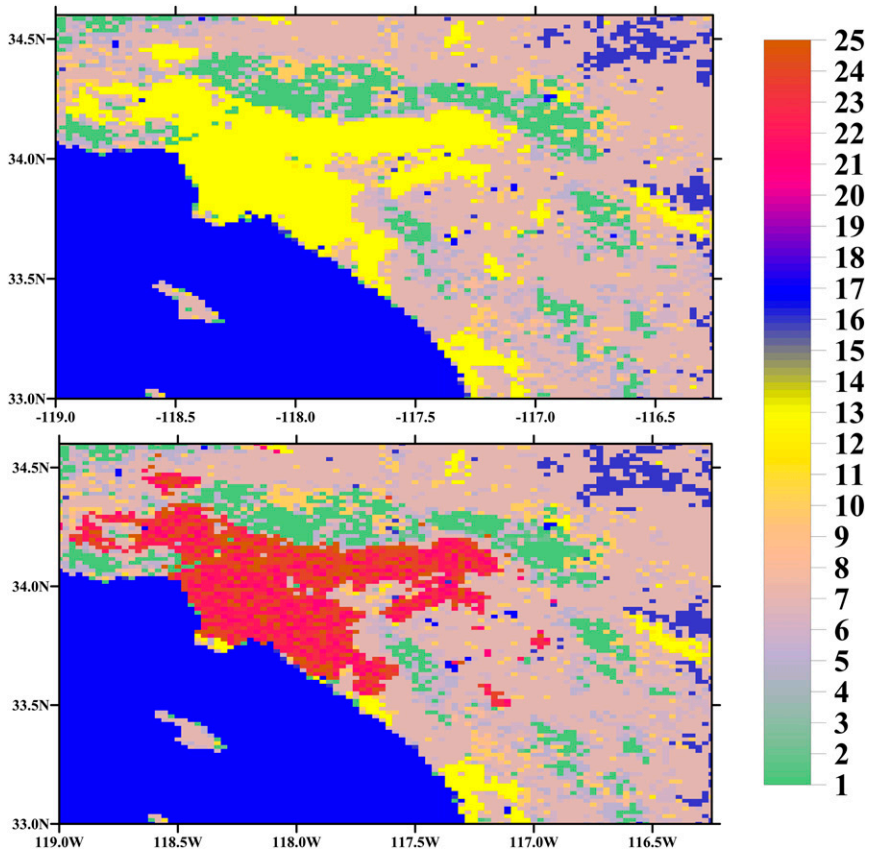

Figure 6. Different land-cover classification scenarios used in the numerical simulations: (top) default MODIS IGBP and (bottom) updated urban classes for MODIS IGBP. The reader is referred to Table 2 for a description of each class number and its corresponding biophysical parameters.

3. Results

3.1. Generation of new land classes and analysis of urban land covers

The bivariate density of the SoCAB urban albedos and LSTs (Figure 8, right) shows that both variables are somewhat evenly distributed around a high urban density center, located approximately at an albedo of 0.14 and LST of 40°C, consistent with other LCLU datasets, which assign an albedo of 0.15 for urban classes. The urban albedos extend from 0.01 to 0.57, with 95% of the pixels showing albedos between 0.07 and 0.24. The urban LSTs are also distributed evenly around their mode with 95% of the data lying between 30° and 50°C. The nonurban classes (Figure 8, left), on the other hand, show a much broader range, particularly on LSTs. This is also expected since this category includes all types of land classes with very different surface characteristics. There is a small cluster of low albedo (less than 0.08) and LST (around 20°C) pixels, which corresponds to

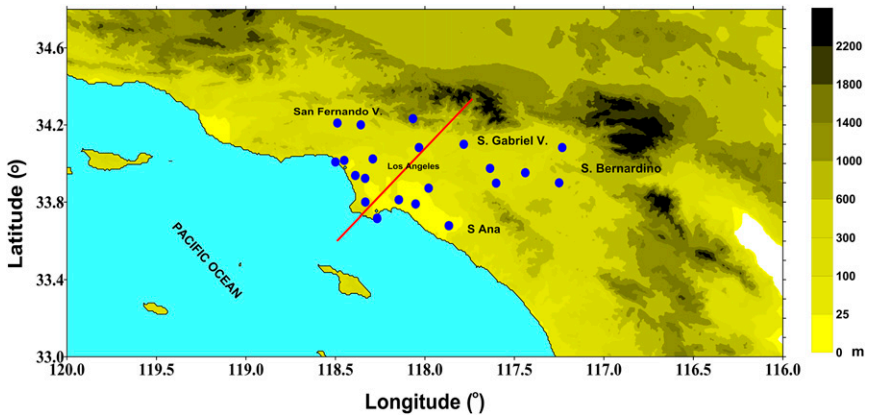

Figure 7. Elevation model (m MSL) and key geographical locations of the region. METAR meteorological ground stations in the region (blue). The red line indicates the cross section used for the vertical profiles in Figure 15.

water. The rest of the land classes have albedos ranging between 0.08 and 0.23 and LSTs from approximately 25° to 52°C.

The average silhouette criterion suggests that the optimum number of urban subclasses according to their albedo is five since it has the highest value when comparing the other number of classes (Table 1). The silhouette (Figure 9) indicates that there are a number of pixels, especially in classes one (1) and five (5), that seem to be misclassified, given by their negative silhouette value; however, these values are considered outliers since they are outside the distribution of their

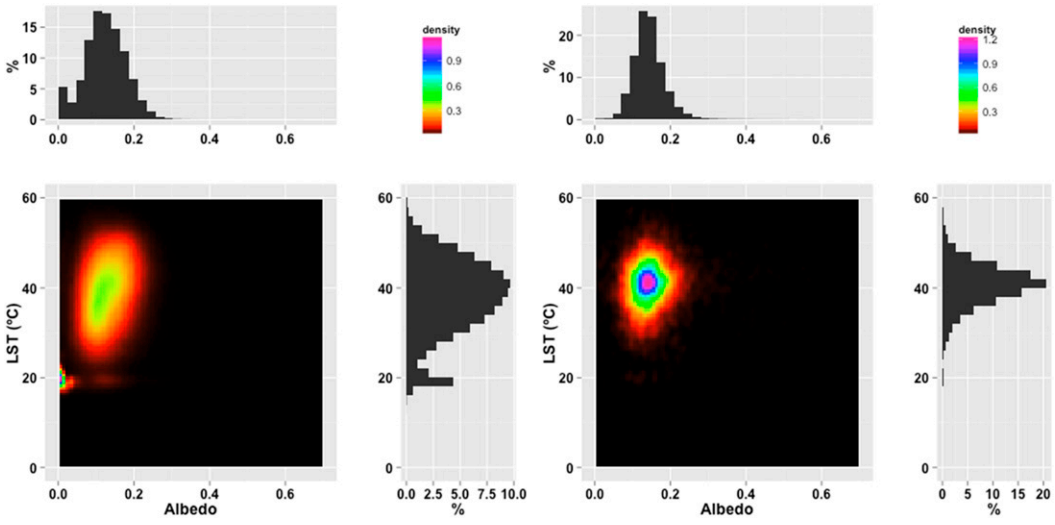

Figure 8. SoCAB albedo vs LST bivariate density and marginal histograms for each variable for (left) nonurban and (right) urban classes.

Table 1. Average silhouette for all new urban classes derived through the CLARA algorithm. Observations with a large silhouette (almost 1) are very well clustered, whereas a small silhouette (around 0) means that the observation lies between two clusters, and observations with a negative silhouette are probably in the wrong cluster.

Number of new urban classes	Average silhouette
3	0.47
4	0.49
5	0.54
6	0.52
7	0.51
8	0.51
9	0.50

own class (Figure 10) and most likely are atypical values for the urban albedos in the region. The albedo versus LST (Figure 11) plot according to the new classification shows that each class is differentiated from one another, and they account for the level of heterogeneity found in the urban landscapes.

Once the SoCAB albedo groups were generated, five new vegetation indices (VIs) were created by combining the SoCAB albedos with the other biophysical

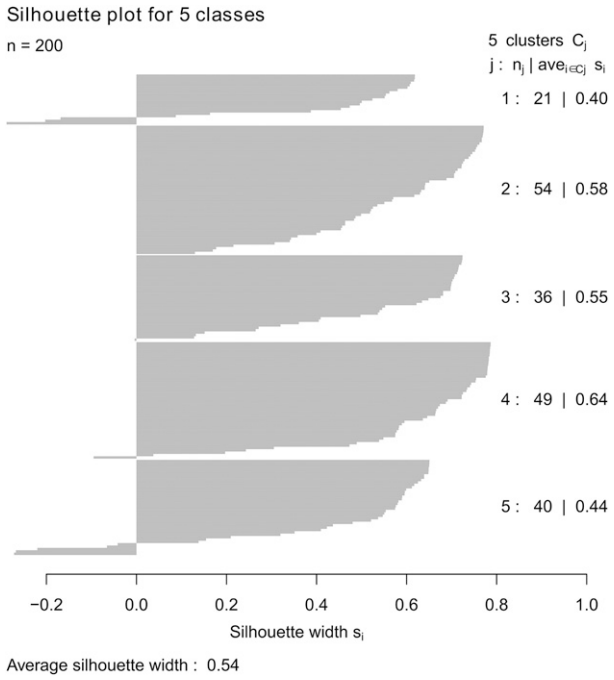

Figure 9. Silhouette for 200 pixels for each one of the five new urban classes. Observations with a large silhouette (almost 1) are very well clustered, whereas a small silhouette (around 0) means that the observation lies between two clusters, and observations with a negative silhouette are probably in the wrong cluster.

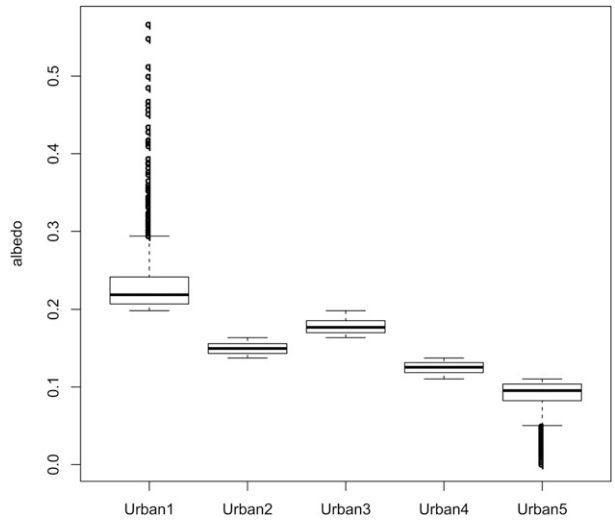

Figure 10. Albedo distribution for each one of the five new urban classes.

parameters of the bare soil and urban/built-up indices (Comarazamy et al. 2010). These new VIs were named urban 1–urban 5. The vegetation parameter table used in WRF's modified land surface model allows for a range of values for each parameter instead of a single one, such that the minimum and maximum albedos for each class were included in the table. The updated high-resolution model will also serve to update the vegetation fraction at each pixel for each of the three WRF grids. Table 2 contains the full list of the VIs and their corresponding parameters.

3.2. Observational analysis of thermal gradient and sea breeze

Understanding the daily spatial and temporal thermal gradient and wind cycle in the region is crucial for assessing the influence of urban landscapes on sea-breeze patterns and coastal cooling.

The general surface wind pattern through the SoCAB is predominantly from the ocean toward the land during the spring, summer, and fall seasons. This flow, however, is considerably influenced by the orientation of the various mountain ranges that surround the area on the north and east. The surface sea-breeze pattern on an average summer day consists of a relatively strong movement inland during the day with peak flow at about 1600 local time (LT), followed by an inversion land-breeze weak movement toward the sea starting in the evening hours (~2200 LT) in a net diurnal onshore air movement (Neiburger and Edinger 1954).

The MASTER-derived LST map (Figure 3, bottom) over the SoCAB on 24 September 2013 shows the typical summer sea–land temperature difference during the late morning hours over the region. At the time of the flight (approximately 1200 LT), the LSTs in the urban areas of Los Angeles and the valleys are over 20°C greater than Pacific Ocean SSTs. This difference reduces to approximately 5°C at the highest points of the San Gabriel and San Bernardino Mountains. At this time

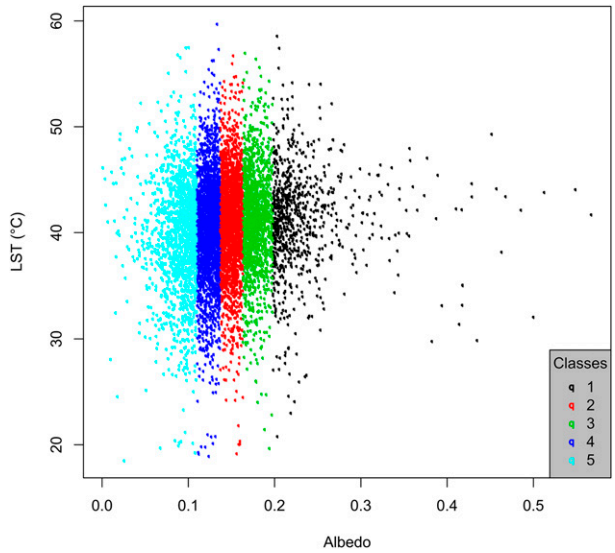

Figure 11. Albedo and LST bivariate distribution for each one of the five new urban classes

of the day, air mass is mixed upward over land by turbulent mixing in the unstable, stratified boundary layer, creating an offshore pressure gradient at some distance above ground. The resultant offshore flow of air above ground near the coast creates a low pressure region at ground level and onshore surface winds (Pielke 2002).

The observed wind speeds at the 18 METAR stations (Figure 12) on the same date also reflect these daily patterns. At 0900 LT, the sea breeze is in its early stages, with coastal stations registering wind speeds from 2 to 5 m s^{-1}, while most inland stations have very weak wind speeds. By 1600 LT the sea breeze is fully developed and has extended inland, with wind speeds reaching up to 9 m s^{-1} in some inland locations. Before sunset, longwave radiative cooling starts dominating over solar heating and the pressure gradient is dissipated by the resulting surface wind, making the sea breeze still present but with lower magnitudes (approximately 3 m s^{-1}) at 2100 LT. As longwave cooling continues, a pressure minimum develops at the coast generating a weak land breeze that is reflected as almost negligible wind speed across the entire region at 0400 LT.

3.3. Model validation

Hourly WRF outputs, produced with parameterization as described in sections 2.3 and 2.4, were compared with average hourly observations from 18 ground stations. The model was validated on a 10-day period from 16 to 26 September 2013 in order to include the day of the flight campaign (24 September 2013).

WRF surface temperatures (Figure 13, top) generally correlate well with observations (coefficient of determination $R^2 = 0.89$; Figure 14) as they capture

Table 2. Biophysical parameters for each of the vegetation indices used by WRF: green vegetation fraction (SHDFAC (fraction 0.0 to 1.0)), rooting depth (NROOT (soil layer index)), stomatal resistance (RS ($s\,m^{-1}$)), parameter used in radiation stress function (RGL (dimensionless)), parameter used in vapor pressure deficit function (HS (dimensionless)), upper bound on maximum albedo over deep snow (MAXALB (%)), minimum leaf area index throughout the year (LAIMIN (dimensionless)), maximum leaf area index throughout the year (LAIMAX (dimensionless)), minimum background emissivity throughout the year (EMISSMIN (fraction 0.0 to 1.0)), maximum background emissivity throughout the year (EMISSMAX (fraction 0.0 to 1.0)), minimum background albedo throughout the year (ALBEDOMIN (fraction 0.0 to 1.0)), maximum background albedo throughout the year (ALBEDOMAX (fraction 0.0 to 1.0)), minimum background roughness length throughout the year (Z0MIN (fraction 0.0 to 1.0)), and maximum background roughness length throughout the year (Z0MAX (fraction 0.0 to 1.0)). Asterisks indicate the new land-cover/land-use classes derived from this study.

No.	SHDFAC	NROOT	RS	RGL	HS	SNUP	MAXALB	LAIMIN	LAIMAX	EMISSMIN	EMISSMAX	ALBEDOMIN	ALBEDOMAX	Z0MIN	Z0MAX	Description
1	0.7	4	125	30	47.35	0.08	52	5	6.4	0.95	0.95	0.12	0.12	0.5	0.5	Evergreen needleleaf forest
2	0.95	4	150	30	41.69	0.08	35	3.08	6.48	0.95	0.95	0.12	0.12	0.5	0.5	Evergreen broadleaf forest
3	0.7	4	150	30	47.35	0.08	54	1	5.16	0.93	0.94	0.14	0.15	0.5	0.5	Deciduous needleleaf forest
4	0.8	4	100	30	54.53	0.08	58	1.85	3.31	0.93	0.93	0.16	0.17	0.5	0.5	Deciduous broadleaf forest
5	0.8	4	125	30	51.93	0.08	53	2.8	5.5	0.93	0.97	0.17	0.25	0.2	0.5	Mixed forests
6	0.7	3	300	100	42	0.03	60	0.5	3.66	0.93	0.93	0.25	0.3	0.01	0.05	Closed shrublands
7	0.7	3	170	100	39.18	0.035	65	0.6	2.6	0.93	0.95	0.22	0.3	0.01	0.06	Open shrublands
8	0.7	3	300	100	42	0.03	60	0.5	3.66	0.93	0.93	0.25	0.3	0.01	0.05	Woody savannas
9	0.5	3	70	65	54.53	0.04	50	0.5	3.66	0.92	0.92	0.2	0.2	0.15	0.15	Savannas
10	0.8	3	40	100	36.35	0.04	70	0.52	2.9	0.92	0.96	0.19	0.23	0.1	0.12	Grasslands
11	0.6	2	70	65	55.97	0.015	59	1.75	5.72	0.95	0.95	0.14	0.14	0.3	0.3	Permanent wetlands

Table 2. (*Continued*)

No.	SHDFAC	NROOT	RS	RGL	HS	SNUP	MAXALB	LAIMIN	LAIMAX	EMISSMIN	EMISSMAX	ALBEDOMIN	ALBEDOMAX	Z0MIN	Z0MAX	Description
12	0.8	3	40	100	36.25	0.04	66	1.56	5.68	0.92	0.985	0.17	0.23	0.05	0.15	Croplands
13	0.1	1	200	999	999	0.04	46	1	1	0.88	0.88	0.15	0.15	0.5	0.5	Urban and built-up
14	0.8	3	40	100	36.25	0.04	68	2.29	4.29	0.92	0.98	0.18	0.23	0.05	0.14	Cropland/ natural vegetation mosaic
15	0	1	999	999	999	0.02	82	0.01	0.01	0.95	0.95	0.55	0.7	0.001	0.001	Snow and ice
16	0.01	1	999	999	999	0.02	75	0.1	0.75	0.9	0.9	0.38	0.38	0.01	0.01	Barren or sparsely vegetated
17	0	0	100	30	51.75	0.01	70	0.01	0.01	0.98	0.98	0.08	0.08	0.0001	0.0001	Water
18	0.6	3	150	100	42	0.025	55	0.41	3.35	0.93	0.93	0.15	0.2	0.3	0.3	Wooded tundra
19	0.6	3	150	100	42	0.025	60	0.41	3.35	0.92	0.92	0.15	0.2	0.15	0.15	Mixed tundra
20	0.3	2	200	100	42	0.02	75	0.41	3.35	0.9	0.9	0.25	0.25	0.05	0.1	Barren tundra
21	0.1	1	200	999	999	0.04	46	1	1	0.88	0.88	0.2	0.28	0.5	0.5	Urban 1*
22	0.1	1	200	999	999	0.04	46	1	1	0.88	0.88	0.14	0.16	0.5	0.5	Urban 2*
23	0.1	1	200	999	999	0.04	46	1	1	0.88	0.88	0.16	0.2	0.5	0.5	Urban 3*
24	0.1	1	200	999	999	0.04	46	1	1	0.88	0.88	0.11	0.14	0.5	0.5	Urban 4*
25	0.1	1	200	999	999	0.04	46	1	1	0.88	0.88	0.07	0.11	0.5	0.5	Urban 5*

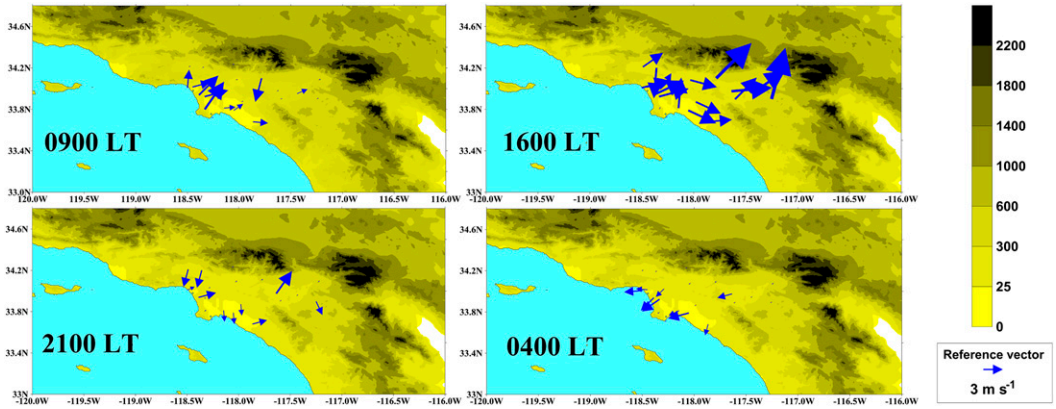

Figure 12. Surface winds vectors ($m\,s^{-1}$) for 18 METAR stations at 0900, 1600, and 2100 LT 24 Sep 2013 and 0400 LT 25 Sep 2013. Color bar indicates topography in meters.

day-to-day trends in average observed peak values. WRF performs particularly well capturing daily maximum surface temperatures, especially in the first 5 days. The model, however, presents a delay in capturing the synoptic event on the fifth simulation day, hence underestimating both maximum and minimum temperatures

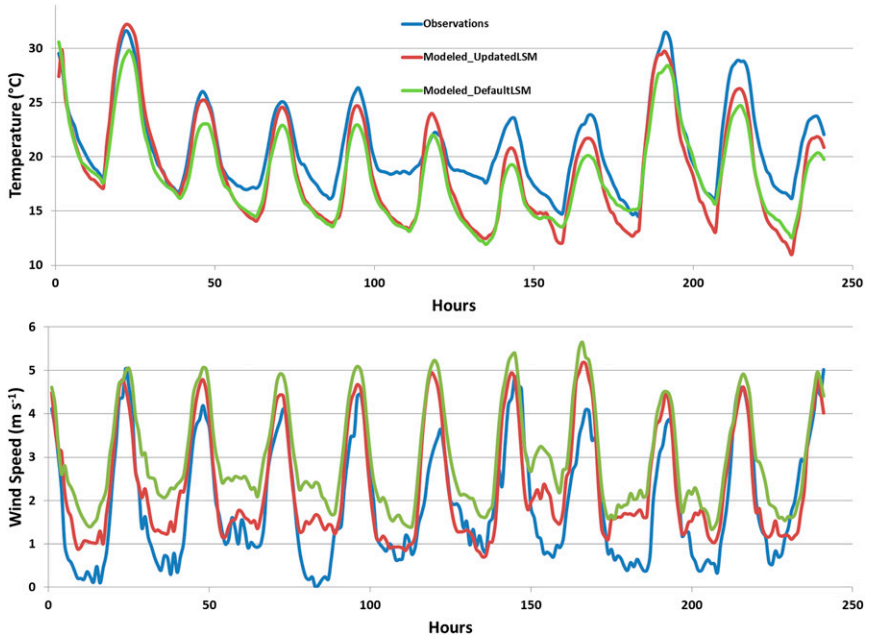

Figure 13. Modeled with updated land classes (red), modeled with default land classes (green), and observed (blue) hourly averaged (over the 18 METAR stations in Figure 7 for 16–26 Sep 2013): (top) 2-m air temperatures (°C) and (bottom) surface wind speeds ($m\,s^{-1}$).

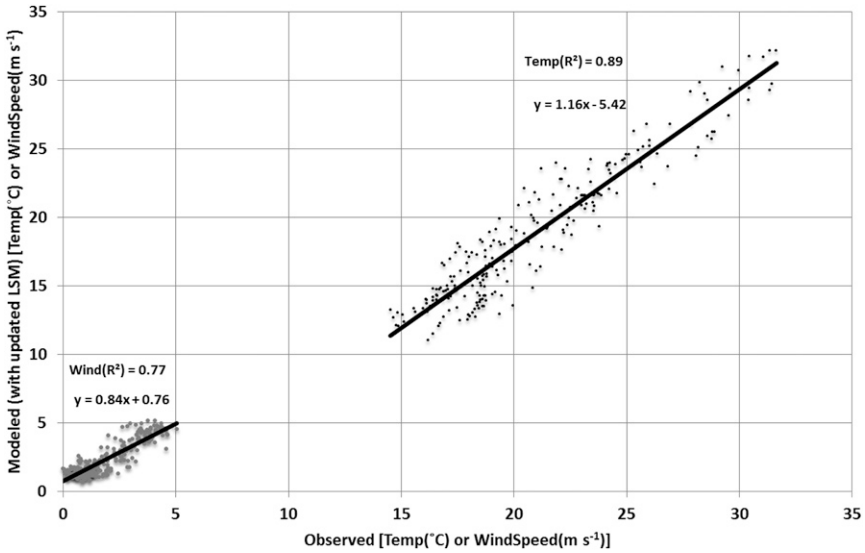

Figure 14. Correlation and trend line equations of observed and modeled with updated land classes' temperatures (black; °C) and wind speeds (gray; m s^{-1}).

on the next 2 days. This delay is mostly a consequence of NCEP forcings. However, the improvement in the modeled results obtained with the new urban classes is very clear at daytime (~2°C), as the results with default land cover consistently underestimate maximum temperatures by as much as 4°C. Minimum temperatures are underestimated by WRF for the two cases except for the first 2 days; this is reflected in a higher average observed temperature (20.9°C) than the average modeled temperature (18.8°C). This is also due to underestimation of minimum temperatures from NCEP. Despite the improvements in maximum temperatures with the new land classes, adding the updated land classes to WRF still results in an underestimation of nighttime temperatures. This underestimation of minimum temperatures may be the result of several factors including changes in surface albedo within the new classes, NCEP forcings, and underestimation of thermal storage of the built environment. We attribute the underestimation of minimum temperatures in the updated land cover mostly to higher regional average urban albedo when using the new urban land classes (~0.17) than when using the default urban albedo (0.15). This translates to less solar energy absorbed by the surface at daytime and consequently lower thermal energy released at nighttime. Other studies have detected this underestimation of minimum temperatures in urban environments (Holt and Pullen 2007; Gutierrez et al. 2014) and successfully compensated the nighttime excessive cooling by adding a more complex urban parameterization that accounts for shadowing and radiation trapping effects and urban anthropogenic heat (Gutierrez et al. 2014).

However, we deem the results to be satisfactory given that the focus of the work is in representing maximum temperatures, and the updated model with new land

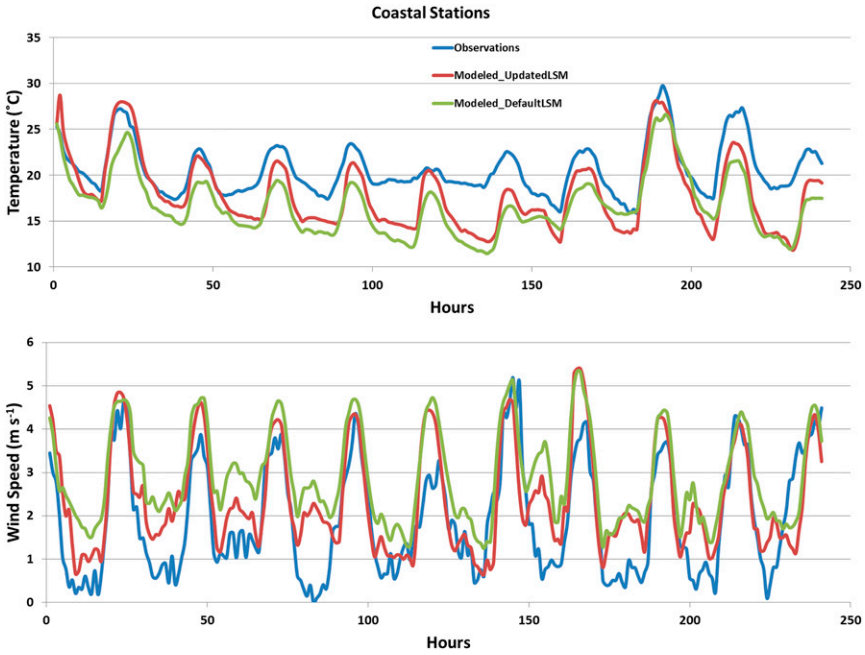

Figure 15. As in Figure 13, but for coastal locations.

classification shows enhanced performance over the default values. These results are not classified into urban and nonurban locations, since only 1 of the 18 ground stations was not located within the urban environment.

The modeled surface wind speeds (Figure 13, bottom) also correlate well with observations ($R^2 = 0.78$; Figure 14). Daily maximum wind speeds are estimated with very small biases (less than $0.5\,\mathrm{m\,s^{-1}}$) in 8 out of the 10 days. The synoptic event of the fifth day is reflected in the overestimations of maximum wind speeds on the fifth and seventh day. Consistent with underestimated minimum temperatures, WRF overestimates nighttime surface winds, particularly in near-calm conditions. This generates an overall slightly higher average modeled wind speed ($2.37\,\mathrm{m\,s^{-1}}$) than the average observed speed ($1.91\,\mathrm{m\,s^{-1}}$). Such stable overestimations of near-calm speeds are common in mesoscale models and are probably related to deficiencies in their PBL schemes (Baklanov et al. 2011). As with surface temperatures, the model with updated urban classes is consistently closer to observed daytime wind speeds than with default urban classes.

The same modeled versus observations time series plots were derived for the nine coastal stations (inland distances less than 30 km; Figure 15) and nine inland stations (inland distances greater than 30 km; Figure 16). Inland daily maximum temperatures are significantly higher (as much as 7°C) than coastal maximum temperatures. This major difference is not seen on wind speeds, as average hourly wind speeds seem to be in the same range for both regions. The most important aspect of these plots is that they show that daytime surface temperatures and wind speeds are better estimated with the updated land classes in both coastal and inland regions.

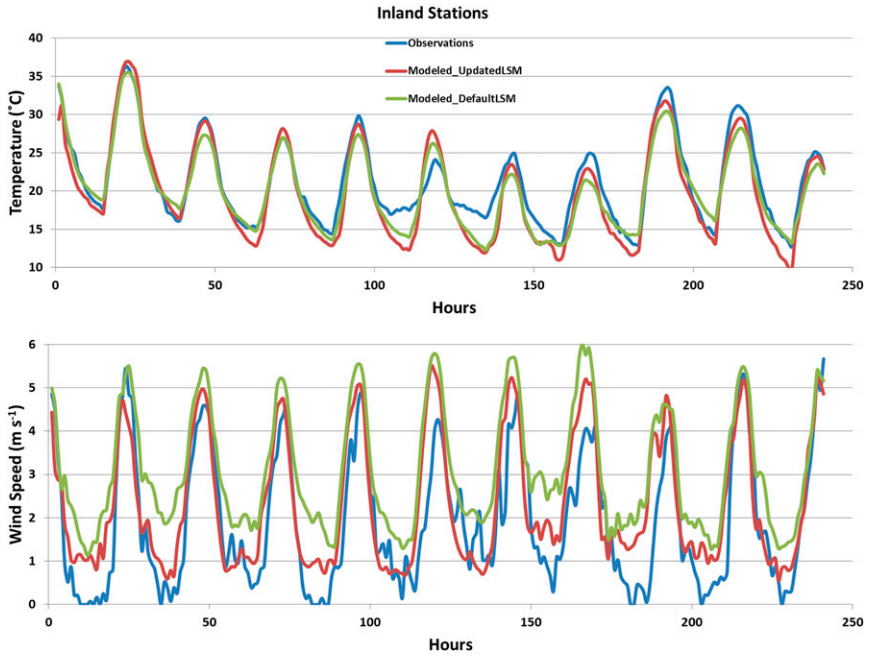

Figure 16. As in Figure 13, but for inland locations.

The improvements of the model due to the new urban land classes are hereby quantified through the root-mean-square error (RMSE; Table 3) between the observations and modeled (with updated and default land classes) daytime temperatures and diurnal sea breezes in coastal and inland locations. The updated land classes improve estimations on daytime temperatures across the entire region since they reduce the RMSE between the observations and modeling results, especially in coastal areas where the updated model decreases the estimation error by more than 1°C and reduces the RMSE by approximately 20%. Similar improvements are also seen on wind speeds as the new land classes reduce the RMSE by 0.38 m s^{-1} (27%) in inland areas and by 0.24 m s^{-1} (24%) in coastal areas.

Additional statistical analyses through hypothesis tests were performed in order to assess if the model improvements were statistically significant and not a result of chance. In that sense, each combination of updated versus default modeled results

Table 3. RMSE between observed and modeled (with both model parameterizations) values for daytime 2-m air temperatures (°C) and diurnal wind speeds (m s^{-1}) in coastal and inland areas. All listed changes in variables between default and updated land classes are statistically significant, with p value < 0.01.

	2-m air temperatures (°C)		Wind speeds (m s^{-1})	
	Coastal	Inland	Coastal	Inland
Default land classes	4.51	2.14	0.98	1.39
Updated land classes	3.29	1.72	0.74	1.01

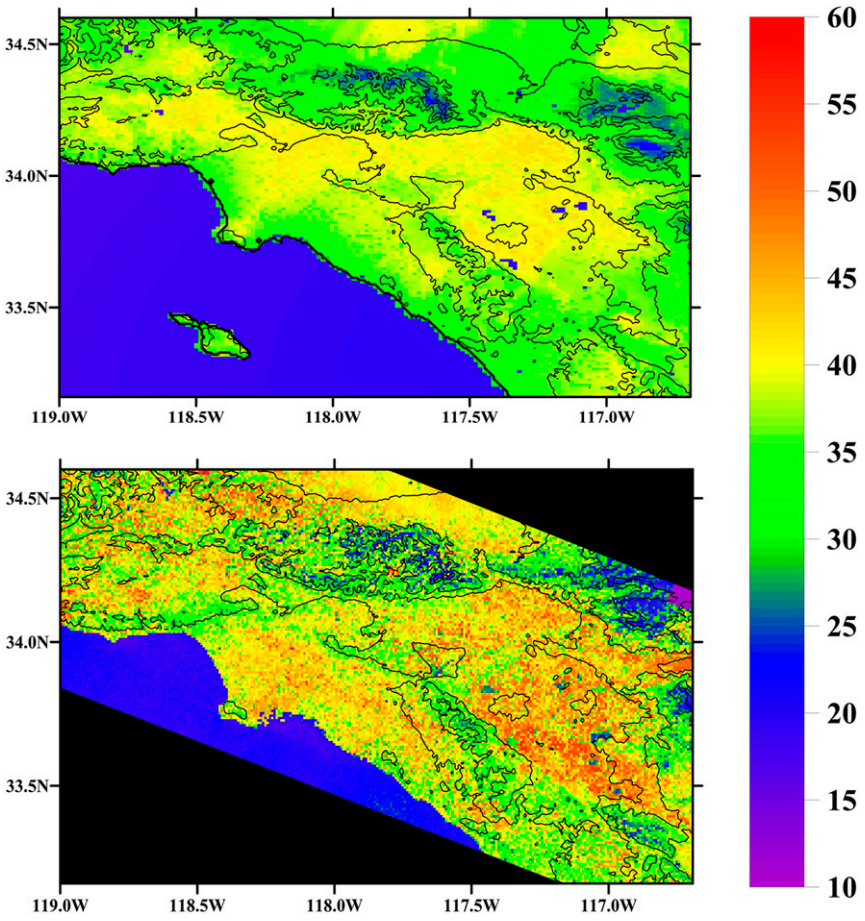

Figure 17. (top) Domain 3 WRF with updated land classes skin temperatures (°C) at the time of the flight and (bottom) MASTER-derived LSTs. Black contour lines indicate key topographic heights. Black regions indicate no data.

were linearly regressed against each other, and a hypothesis test was performed on the slope coefficient. The null hypothesis for this test states that the slope coefficient of the two different models regressed against each other is equal to 1, indicating that both land schemes provide the same output. The p value is the probability, under the null hypothesis, that the calculated value of the test statistic will occur by chance. Therefore, the null hypothesis is rejected if the p value is less than or equal to the test significance level. Given that the p value is less than 0.01 for every test (not shown), it is clear that there is a statistically significant difference between the daytime temperatures and diurnal wind speeds estimated under both model parameterizations at typical significance levels. Moreover, the difference is statistically significant in both coastal and inland areas.

The two previous analyses are key in this study as they lead to the following conclusions: First, the updated model improves daytime temperature and diurnal wind speed estimations for both coastal and inland areas, as it reduces the RMSE when comparing with the default model estimations in all cases. Second, such

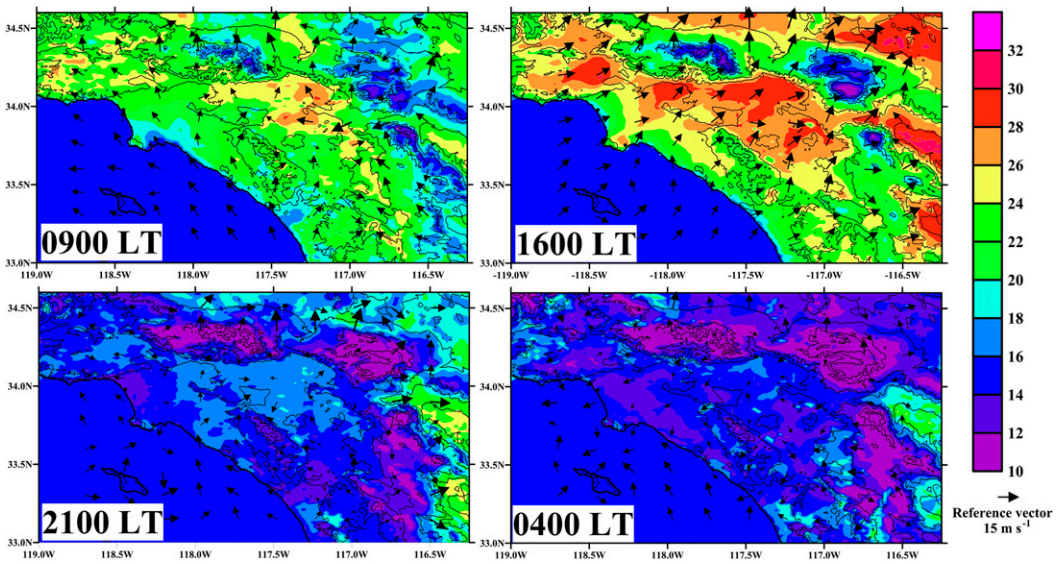

Figure 18. Domain 3 WRF with updated land classes 2-m air temperature (°C) and 10-m wind speeds (reference vector in lower-right corner of each figure; m s^{-1}) at 0900, 1600, and 2100 LT 24 Sep 2013 and 0400 LT 25 Sep 2013. Black contour lines indicate key topographic heights.

improvements on the physics of the model are statistically significant and not a result of chance.

Skin temperatures modeled with the new urban classes also correlate well with MASTER-derived LSTs at the time of the flight (Figure 17, bottom) since the model was able to reproduce a spatial pattern of heating similar to the one observed by MASTER. The model successfully captures the lower temperatures at higher elevations and maximum heating at urban areas even though the MASTER LSTs are far more heterogeneous than the modeled results. This is expected given the higher resolution of the airborne data (35 m) in comparison to the modeling grid (1 km). Relatively colder land temperatures by the model are mainly due to the cold SSTs used near the coast, assimilated from the boundary conditions at a 1° grid resolution. Whereas WRF outputs over the entire region are estimated at a fixed time, the flight data were collected over the same domain during the course of 4 h, giving rise to major temperature differences in some regions, particularly in the southernmost part of the domain where the temperatures were observed approximately 2 h later than the WRF output.

3.4. Modeled horizontal and vertical temperature and wind structure

The surface spatial and temporal patterns of daily temperature and wind patterns are presented here by means of WRF surface temperature and wind outputs (Figure 18) for the day of the flight campaign (24 September 2013). After sunrise, at 0900 LT, onshore surface winds start developing on the coast toward the

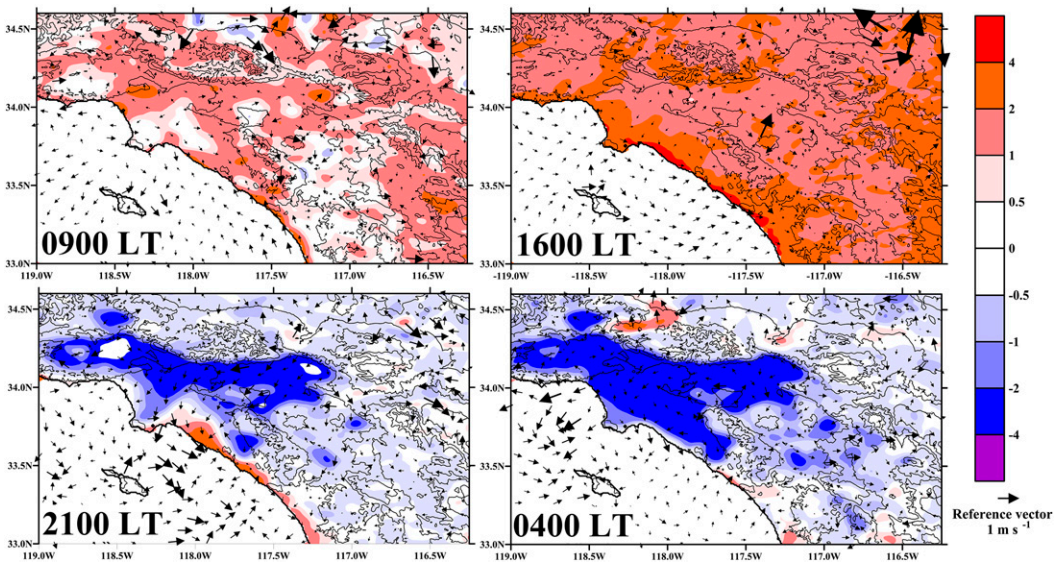

Figure 19. Domain 3 WRF difference (updated minus default land classes) 2-m air temperature (°C) and 10-m wind speeds (reference vector in lower-right corner of each figure; m s^{-1}) at 0900, 1600, and 2100 LT 24 Sep 2013 and 0400 LT 25 Sep 2013. Black contour lines indicate key topographic heights.

mountains at average speeds of approximately 2 m s^{-1}; at this time, surface temperatures are approximately 6°C higher than SSTs at downtown Los Angeles and 8°–10°C higher in the valleys. The maximum sea breeze is reached at 1600 LT; here, the flow is mostly west-southwest with magnitudes of approximately 7 m s^{-1} and a more uniform land–sea temperature difference of 10°C across the region. At 2100 LT, the sea breeze is still present over much of the area but greatly reduced ($<$1 m s^{-1}), with no temperature differences between land and ocean. After this hour, winds start changing direction, and at 0400 LT of the next day, the time of maximum land breeze, the air movement is somewhat uniform from the coastal valleys across the plain toward the western coast line, with average wind speeds of approximately 1 m s^{-1}. These patterns are in agreement with previous daily circulation pattern studies for the region (Neiburger and Edinger 1954; Bruno et al. 2000; Lebassi-Habtezion et al. 2011). It is important to notice that despite the spatial heterogeneity of the new urban classes (Figure 6), the spatial distribution of the surface temperatures is smooth at all times and does not show many sharp, local variations.

A key aspect in this study is the analysis of the impacts of the new urban classes on the spatial distribution of temperatures, both horizontally and vertically, as well as the timing and strength of the sea breeze. Figure 19 shows the difference in WRF surface temperatures and winds for the day of the flight campaign (24 September 2013) between the updated and the default land classes. Surface daytime temperatures are also similar in terms of magnitude and spatial distribution. The impact of the new land classes on surface temperatures are very clear at both daytime

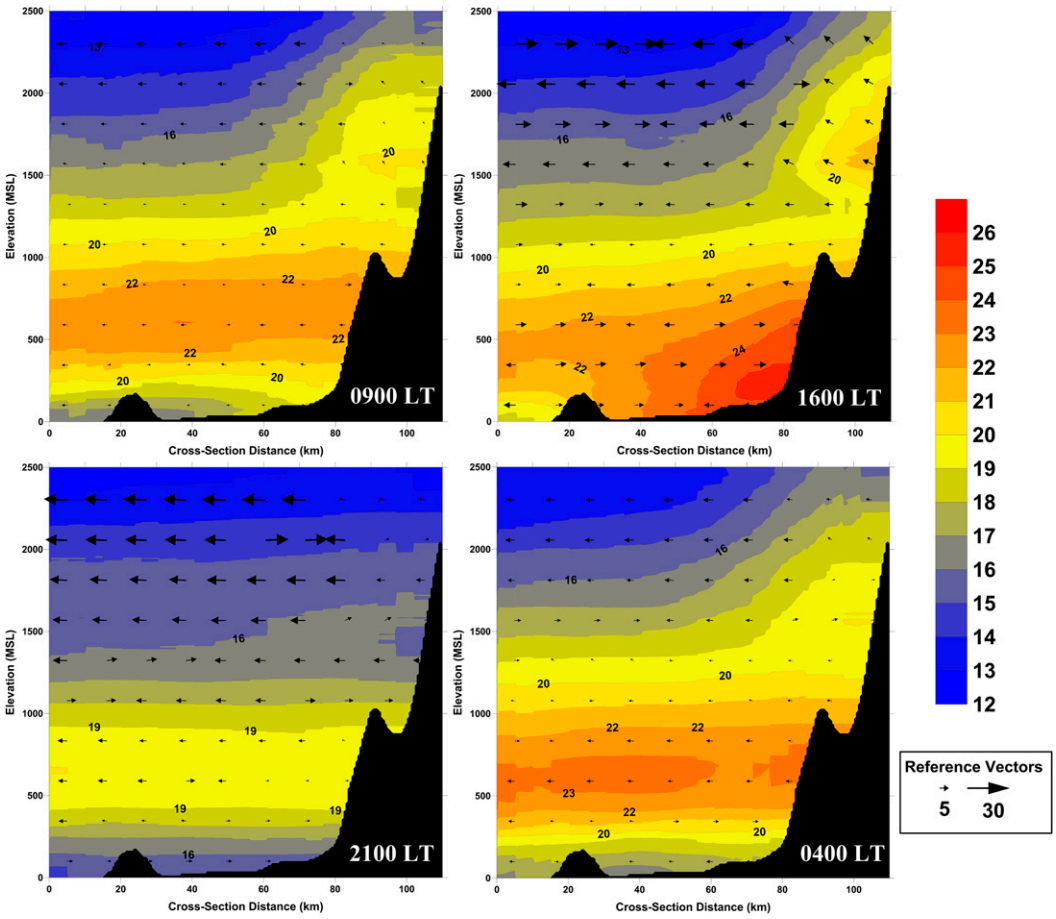

Figure 20. Domain 3 WRF with updated land classes vertical temperature (°C) and wind (reference vector in the lower-right corner; m s^{-1}) profiles for the cross section in Figure 7 at 0900, 1600, and 2100 LT 24 Sep 2013 and 0400 LT 25 Sep 2013. Black area corresponds to topography. Elevation in m MSL.

and nighttime. At 0900 LT, the entire region shows increases in temperatures as much as 2°C when comparing the updated model with the default one. Such increases are even higher at 1600 LT, with an average regional increase of approximately 2°C and a maximum increase of 4°C along the coastline.

It is important to notice also that the effects of these new classes are detected across the entire region and are not constrained solely to the urban extent, as reported in other studies (Carter et al. 2012). Nighttime surface temperatures, however, show notable discrepancies between both models, especially at 0400 LT, where the default land surface model shows higher temperatures (as much as a 4°C difference) than the updated model in downtown Los Angeles and the valleys. As discussed previously, overall lower nighttime surface temperatures in the updated model might be due to the decrease in longwave emission generated by the overall higher albedo in the new urban classes. The surface winds also show discrepancies

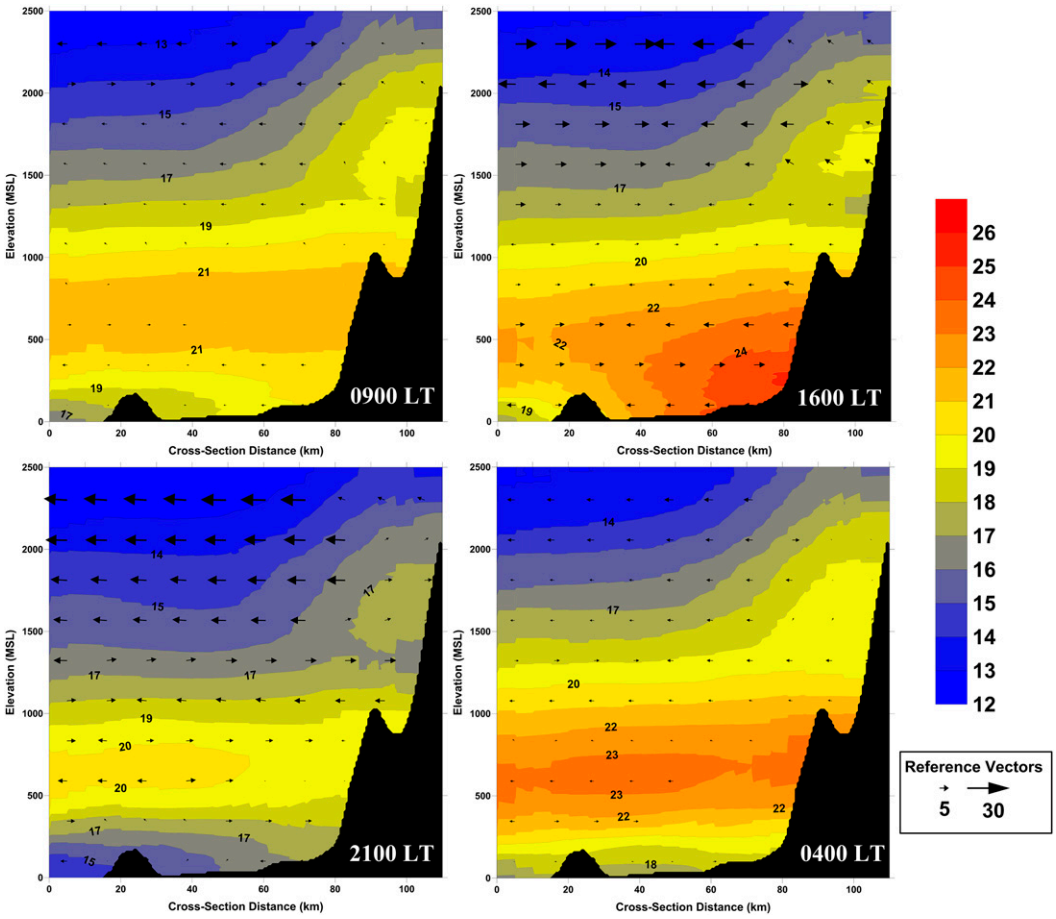

Figure 21. As in Figure 20, but with default land classes.

between models with overall higher differences at nighttime ($\sim 1\ \mathrm{m\ s^{-1}}$) when comparing to daytime wind speeds ($\sim 0.5\ \mathrm{m\ s^{-1}}$).

The vertical temperatures and daily wind for the updated land classes are shown in Figure 20 over the cross section in Figure 7. The marine boundary layer (MBL) is still at full inland extent at 0900 LT, with a subsidence inversion top at about 700 m AGL and at a temperature between 22° and 23°C. At 1600 LT, the time of the maximum sea-breeze intensity, the MBL extends only 20 km inland because of turbulent mixing over land during the late morning hours. The inversion occurs at 500 m AGL between 22° and 23°C. In addition to the onshore air flows near the surface, there are offshore winds above the inversion top because of the expansion of the air column over land. After sunset, the lowest atmospheric layer cools again, restoring the MBL to its full inland extent by 2100 LT. At this time, the inversion top goes back to 700 m and occurs at 20°C. At 0400 LT, the near-surface offshore winds (land breeze) have developed in response to the loss of mass above the surface over water. Overall, the same daytime temperature and wind patterns are also observed in the simulations performed with the default land surface model (Figure 21), especially at higher

altitudes where the new land classes are not expected to have a significant impact. The main difference between both simulations occurs at 2100 LT; at this time, the MBL extends 50 km inland with the default land classes, while it has already reached its full inland extent with the new urban classes. The air temperatures near the ground are also slightly higher (~2°C) with the default land classes. This difference in timing in the restoration of the full MBL indicates that longwave radiation cooling was more dominant with the new urban classes, lowering surface and near-ground air temperatures faster than the default land classes. This effect is also attributed to the overall higher albedos in the new urban classes.

4. Conclusions and future works

Understanding the mechanisms of the urban heat island (UHI) is key in representing regional climate dynamics, particularly in coastal cities, where the UHI influences merge with large-scale atmospheric and oceanic circulation patterns. The Southern California air basin (SoCAB) is of particular interest, given reported coastal cooling for the region attributed to GHG-induced warming (Lebassi et al. 2009). To estimate the impacts of urbanization on surface temperatures and daily sea-breeze patterns, a new land-cover classification scheme was derived for the SoCAB using updated airborne remote sensing data from the recent HyspIRI mission preparatory flight campaigns. This new land surface model was then validated for use in long-term modeling studies.

A mesoscale model (WRF) validation was carried out to assess the suitability of a numerical modeling configuration with updated urban land classes in estimating summer surface 2-m air daytime temperatures and wind speeds for the region.

The model's surface characteristics were updated by including five new urban land classes. These urban classes were obtained by means of the CLARA algorithm using broadband albedo derived from the AVIRIS sensor during the HyspIRI mission preparatory flight campaigns over Southern California. The SoCAB urban albedos are distributed symmetrically around a mode of 0.14 with 95% of the pixels showing albedos between 0.07 and 0.24 and LSTs between 30° and 50°C. The nonurban land classes in the region have a similar range of albedos and a broader range for LST, with albedos ranging between 0.08 and 0.23 and LSTs from approximately 25° to 52°C.

The MASTER land surface temperature (LST) map, collected at approximately 1200 local time (LT) 24 September 2013 over the area of interest, showed land–sea surface temperature differences on the order of 20°C for much of the domain. The observed wind speeds from 18 ground stations reflected the thermal response to this gradient through an increase in sea-breeze wind speeds from 2 to 5 $m\,s^{-1}$ at coastal sites only at 0900 LT to 9 $m\,s^{-1}$ in coastal and inland locations at 1600 LT.

The mesoscale model configuration was successfully validated since it captured daily cycles and peak values of surface temperature and wind speeds in the SoCAB when compared to observations for a 10-day period. The updated urban land cover largely improved the model's predictions at daytime, especially in temperature, since it notably reduced the biases obtained with the default land-cover classification in WRF (by as much as 4°C). These results reaffirm the importance of properly modeling the urban surface physical properties and incorporating the

heterogeneity of the urban landscape since they have a direct impact on climate variables. In that sense, satellite-based land class updates using HysPIRI preparation flights provide a tool that can greatly improve impacts due to urbanization at global cities, serving as substitutes for locally based urban parameterizations.

When compared to previous observational studies in the region, the horizontal and vertical temporal pattern of the daily sea- and land-breeze cycle was captured by WRF in both magnitude and the direction of the prevalent summer flow patterns. The new urban classes, however, do not perform as well at nighttime as they consistently underestimate minimum temperatures. This error is attributed mainly to an average increase of the new urban albedos, which translates to less solar energy absorbed by the surface at daytime and increased radiation surface cooling of the new land classes.

These results confirm the importance of adding the new urban classes as they showed improvements in daytime surface temperatures and wind speeds, providing a more adequate representation of the surface processes and making the updated land surface model more suitable for long-term maximum temperature and diurnal sea-breeze modeling studies than the default model. Moreover, additional statistical analysis showed that such improvements were systematic and statistically significant for both daytime temperatures and diurnal wind speeds in coastal and inland regions.

The ultimate goal of implementing this methodology is to provide a framework to extend this type of study on a global scale, especially in other regions experiencing similar coastal cooling effects, for example, Chile (Falvey and Garreaud 2009) and Peru (Gutierrez et al. 2011). The additional classification of the urban landscape using remote sensing data also opens the possibilities of studying societal implications of these changes, such as UHI mitigation (Comarazamy et al. 2015), changes in energy demands, air quality, the wine industry, agricultural crops, and other sensitive ecosystems.

Acknowledgments. This work was made possible in part by the following supporting agencies: U.S. National Oceanic and Atmospheric Administration, Office of Education Educational Partnership Program Award NA11SEC4810004; U.S. National Science Foundation under Grant Numbers AGS-1062934 and 0933414; and U.S. Department of Education under Grant P031M105066. This research was also supported, in part, under National Science Foundation Grants CNS-0958379 and CNS-0855217 and the City University of New York High Performance Computing Center at the College of Staten Island.

References

Arnfield, A. J., 2003: Two decades of urban climate research: A review of turbulence, exchanges of energy and water, and the urban heat island. *Int. J. Climatol.*, **23**, 1–26, doi:10.1002/joc.859.

Baklanov, A., and Coauthors, 2011: On the nature, theory, and modeling of atmospheric planetary boundary layers. *Bull. Amer. Meteor. Soc.*, **92**, 123–128, doi:10.1175/2010BAMS2797.1.

Bakun, A., 1990: Global climate change and intensification of coastal ocean upwelling. *Science*, **247**, 198–201, doi:10.1126/science.247.4939.198.

Berk, A., and Coauthors, 2005: MODTRAN 5: A reformulated atmospheric band model with auxiliary species and practical multiple scattering options: Update. *Algorithms and Technologies for Multispectral, Hyperspectral, and Ultraspectral Imagery XI*, S. S. Sylvia and

P. E. Lewis, Eds., International Society for Optical Engineering (SPIE Proceedings, Vol. 5806), doi:10.1117/12.606026.

Bonfils, C., and D. Lobell, 2007: Empirical evidence for a recent slowdown in irrigation-induced cooling. *Proc. Natl. Acad. Sci. USA*, **104**, 13 582–13 587, doi:10.1073/pnas.0700144104.

Bruno, D., G. Ryan, and C. Kaplan, 2000: Climate of Los Angeles, California. NOAA Tech. Memo. NWS WR-261, 173 pp.

Carter, M., J. M. Shepherd, S. Burian, and I. Jeyachandran, 2012: Integration of lidar data into a coupled mesoscale–land surface model: A theoretical assessment of sensitivity of urban–coastal mesoscale circulations to urban canopy parameters. *J. Atmos. Oceanic Technol.*, **29**, 328–346, doi:10.1175/2011JTECHA1524.1.

Cayan, D. R., E. P. Maurer, M. D. Dettinger, M. Tyree, and K. Hayhoe, 2008: Climate change scenarios for the California region. *Climatic Change*, **87**, 21–42, doi:10.1007/s10584-007-9377-6.

Chase, T. N., R. A. Pielke Sr., T. G. F. Kittel, R. R. Nemani, and S. W. Running, 2000: Simulated impacts of historical land cover changes on global climate in northern winter. *Climate Dyn.*, **16**, 93–105, doi:10.1007/s003820050007.

Chen, F., and J. Dudhia, 2001: Coupling an advanced land surface–hydrology model with the Penn State–NCAR MM5 modeling system. Part I: Model implementation and sensitivity. *Mon. Wea. Rev.*, **129**, 569–585, doi:10.1175/1520-0493(2001)129<0569:CAALSH>2.0.CO;2.

Christy, J. R., W. B. Norris, K. Redmond, and K. P. Gallo, 2006: Methodology and results of calculating central California surface temperature trends: Evidence of human-induced climate change? *J. Climate*, **19**, 548–563, doi:10.1175/JCLI3627.1.

Clark, R., 2010: California climate change is caused by the Pacific decadal oscillation, not by carbon dioxide. Science and Public Policy Institute Paper, 22 pp. [Available online at http://scienceandpublicpolicy.org/images/stories/papers/originals/pacific_decadal.pdf.]

Comarazamy, D. E., J. E. Gonzalez, J. C. Luvall, D. L. Rickman, and P. J. Mulero, 2010: A land–atmospheric interaction study in the coastal tropical city of San Juan, Puerto Rico. *Earth Interact.*, **14**, doi:10.1175/2010EI309.1.

——, ——, ——, ——, and R. D. Bornstein, 2013: Climate impacts of land-cover and land-use changes in tropical islands under conditions of global climate change. *J. Climate*, **26**, 1535–1550, doi:10.1175/JCLI-D-12-00087.1.

——, ——, and ——, 2015: Quantification and mitigation of long-term impacts of urbanization and climate change in the tropical city of San Juan, Puerto Rico. Int. *J. Low-Carbon Technol.*, **10**, 87–97, doi:10.1093/ijlct/ctt059.

Cordero, E. C., W. Kessomkiat, J. Abatzoglou, and S. A. Mauget, 2011: The identification of distinct patterns in California temperature trends. *Climatic Change*, **108**, 357–382, doi:10.1007/s10584-011-0023-y.

Dai, A., K. E. Trenbert, and T. R. Karl, 1999: Effects of clouds, soil moisture and water vapor on diurnal temperature range. *J. Climate*, **12**, 2451–2473, doi:10.1175/1520-0442(1999)012<2451:EOCSMP>2.0.CO;2.

Dandou, A., M. Tombrou, and N. Soulakellis, 2009: The influence of the city of Athens on the evolution of the sea-breeze front. *Bound.-Layer Meteor.*, **131**, 35–51, doi:10.1007/s10546-008-9306-x.

Diem, J. E., C. E. Ricketts, and J. R. Dean, 2006: Impacts of urbanization on land-atmosphere carbon exchange within a metropolitan area in the USA. *Climate Res.*, **30**, 201–213, doi:10.3354/cr030201.

Douville, H., 2003: Assessing the influence of soil moisture on seasonal climate variability with AGCMs. *J. Hydrometeor.*, **4**, 1044–1066, doi:10.1175/1525-7541(2003)004<1044:ATIOSM>2.0.CO;2.

Dudhia, J., 1989: Numerical study of convection observed during the winter monsoon experiment using a mesoscale two-dimensional model. *J. Atmos. Sci.*, **46**, 3077–3107, doi:10.1175/1520-0469(1989)046<3077:NSOCOD>2.0.CO;2.

Duffy, P. B., C. Bonfils, and D. Lobell, 2007: Interpreting recent temperature trends in California. *Eos, Trans. Amer. Geophys. Union*, **88**, 409–410, doi:10.1029/2007EO410001.

Falvey, M., and R. Garreaud, 2009: Regional cooling in a warming world: Recent temperature trends in the southeast Pacific and along the west coast of subtropical South America (1979–2006). *J. Geophys. Res.*, **114**, D04102, doi:10.1029/2008JD010519.

Friedl, M. A., D. Sulla-Menashe, B. Tan, A. Schneider, N. Ramankutty, A. Sibley, and X. Huang, 2010: MODIS Collection 5 global land cover: Algorithm refinements and characterization of new datasets. *Remote Sens. Environ.*, **114**, 168–182, doi:10.1016/j.rse.2009.08.016.

Gao, B.-C., and C. O. Davis, 1997: Development of a line-by-line-based atmosphere removal algorithm for airborne and spaceborne imaging spectrometers. *Imaging Spectrometry III*, M. R. Descour and S. S. Shen, Eds., International Society for Optical Engineering (SPIE Proceedings, Vol. 3118), 132–141, doi:10.1117/12.283822.

——, and R. Green, 2010: HyspIRI visible to short wavelength infrared (VSWIR) land surface reflectance. Algorithm Theoretical Basis Document (ATBD), 31 pp. [Available online at https://hyspiri.jpl.nasa.gov/downloads/Algorithm_Theoretical_Basis/HyspIRI_Gao_ATBD-VSWIR_Land_4_2010_101109.pdf.]

——, K. B. Heidebrecht, and A. F. H. Goetz, 1993: Derivation of scaled surface reflectances from AVIRIS data. *Remote Sens. Environ.*, **44**, 165–178, doi:10.1016/0034-4257(93)90014-O.

Gillespie, A., S. Rokugawa, T. Matsunaga, J. S. Cothern, S. Hook, and A. B. Kahle, 1998: A temperature and emissivity separation algorithm for Advanced Spaceborne Thermal Emission and Reflection Radiometer (ASTER) images. *IEEE Trans. Geosci. Remote Sens.*, **36**, 1113–1126, doi:10.1109/36.700995.

Giridharan, R., S. Ganesan, and S. S. Y. Lau, 2004: Daytime urban heat island effect in high-rise and high-density residential developments in Hong Kong. *Energy Build.*, **36**, 525–534, doi:10.1016/j.enbuild.2003.12.016.

Gutierrez, D., and Coauthors, 2011: Coastal cooling and increased productivity in the main upwelling zone off Peru since the mid-twentieth century. *Geophys. Res. Lett.*, **38**, L07603, doi:10.1029/2010GL046324.

Gutierrez, E., J. E. Gonzalez, A. Martili, R. Bornstein, and M. Arend, 2015: Simulations of a heatwave event in New York City using a multilayer urban parametrization. *J. Appl. Meteor. Climatol.*, **54**, 283–301, doi:10.1175/JAMC-D-14-0028.1.

Holt, T., and J. Pullen, 2007: Urban canopy modeling of the New York City metropolitan area: A comparison and validation of single- and multilayer parameterizations. *Mon. Wea. Rev.*, **135**, 1906–1930, doi:10.1175/MWR3372.1.

Hook, S., J. J. Myers, K. J. Thome, M. Fitzgerald, and A. B. Kahle, 2001: The MODIS/ASTER Airborne Simulator (MASTER)—A new instrument for earth science studies. *Remote Sens. Environ.*, **76**, 93–102, doi:10.1016/S0034-4257(00)00195-4.

Hulley, G., and S. Hook, 2011: HyspIRI Level-2 TIR surface radiance algorithm theoretical basis document. JPL Publication 11-1, 35 pp. [Available online at https://hyspiri.jpl.nasa.gov/downloads/Algorithm_Theoretical_Basis/HyspIRI_L2_Surface_Radiance_JPL_Pub_11-1.pdf.]

Jin, J., N. L. Miller, and N. Schlegel, 2010: Sensitivity study of four land surface schemes in the WRF model. *Adv. Meteor.*, **2010**, 167436, doi:10.1155/2010/167436.

Kalnay, E., and M. Cai, 2003: Impact of urbanization and land-use change on climate. *Nature*, **423**, 528–531, doi:10.1038/nature01675.

——, and Coauthors, 1996: The NCEP/NCAR 40-Year Reanalysis Project. *Bull. Amer. Meteor. Soc.*, **77**, 437–471, doi:10.1175/1520-0477(1996)077<0437:TNYRP>2.0.CO;2.

Karl, T. R., and Coauthors, 1993: A new perspective on recent global warming: Asymmetric trends of daily maximum temperature. *Bull. Amer. Meteor. Soc.*, **74**, 1007–1023, doi:10.1175/1520-0477(1993)074<1007:ANPORG>2.0.CO;2.

Kaufman, L., and P. J. Rousseeuw, 1990: *Finding Groups in Data: An Introduction to Cluster Analysis*. Wiley, 342 pp.

Kitada, T., K. Okamura, and S. Tanaka, 1998: Effects of topography and urbanization on local winds and thermal environment in the Nohbi Plain, coastal region of central Japan: A numerical analysis by mesoscale meteorological model with a k−ε turbulence model. *J. Appl. Meteor.*, **37**, 1026–1046, doi:10.1175/1520-0450(1998)037<1026:EOTAUO>2.0.CO;2.

Krayenhoff, E. S., and J. A. Voogt, 2010: Impacts of urban albedo increase on local air temperature at daily–annual time scales: Model results and synthesis of previous work. *J. Appl. Meteor. Climatol.*, **49**, 1634–1648, doi:10.1175/2010JAMC2356.1.

Kusaka, H., F. Kimura, H. Hirakuchi, and M. Mizutori, 2000: The effects of land-use alteration on the sea breeze and daytime heat island in the Tokyo metropolitan area. *J. Meteor. Soc. Japan*, **78**, 405–420.

LaDochy, S., J. Brown, W. Patzert, and M. Selke, 2004: Can U.S. West Coast climate be forecast? Preprints, *Symp. on Forecasting the Weather and Climate of the Atmosphere and Ocean*, Seattle, WA, Amer. Meteor. Soc., P2.1. [Available online at https://ams.confex.com/ams/84Annual/techprogram/paper_71130.htm.]

——, R. Medina, and W. Patzert, 2007: Recent California climate variability: Spatial and temporal patterns in temperature trends. *Inter-Res. Climate Res.*, **33**, 159–169, doi:10.3354/cr033159.

Lebassi, B., J. González, D. Fabris, E. Maurer, N. Miller, C. Milesi, P. Switzer, and R. Bornstein, 2009: Observed 1970–2005 cooling of summer daytime temperatures in coastal California. *J. Climate*, **22**, 3558–3573, doi:10.1175/2008JCLI2111.1.

Lebassi-Habtezion, B., J. González, and R. Bornstein, 2011: Modeled large-scale warming impacts on summer California coastal-cooling trends. *J. Geophys. Res.*, **116**, D20114, doi:10.1029/2011JD015759.

Lo, J. C. F., A. K. H. Lau, F. Chen, J. C. H. Fung, and K. K. M. Leung, 2007: Urban modification in a mesoscale model and the effects on the local circulation in the Pearl River Delta region. *J. Appl. Meteor. Climatol.*, **46**, 457–476, doi:10.1175/JAM2477.1.

McGregor, H. V., M. Dima, H. W. Fischer, and S. Mulitzal, 2007: Rapid 20th-century increase in coastal upwelling off northwest Africa. *Science*, **315**, 637–639, doi:10.1126/science.1134839.

Mintz, Y., 1984: The sensitivity of numerically simulated climates to land-surface boundary conditions. *The Global Climate*, J. T. Houghton, Ed., Cambridge University Press, 79–105.

Nakanishi, M., and H. Niino, 2004: An improved Mellor–Yamada level 3 model with condensation physics: Its design and verification. *Bound.-Layer Meteor.*, **112**, 1–31, doi:10.1023/B:BOUN.0000020164.04146.98.

Neiburger, M., and J. Edinger, 1954: Summary report on the meteorology of the Los Angeles basin with particular respect to the ''smog'' problem. Air Pollution Foundation Tech. Rep., 108 pp.

Nemani, R. R., M. A. White, D. R. Cayan, G. V. Jones, S. W. Running, and J. C. Coughlan, 2001: Asymmetric warming over coastal California and its impact on the premium wine industry. *Climate Res.*, **19**, 25–34, doi:10.3354/cr019025.

Ohashi, Y., and H. Kida, 2002: Local circulations developed in the vicinity of both coastal and inland urban areas: A numerical study with a mesoscale atmospheric model. *J. Appl. Meteor.*, **41**, 30–45, doi:10.1175/1520-0450(2002)041<0030:LCDITV>2.0.CO;2.

Oke, T. R., 1982: The energetic basis of the urban heat island. *Quart. J. Roy. Meteor. Soc.*, **108**, 1–24, doi:10.1002/qj.49710845502.

——, 1984: Methods in urban climatology. *Applied Climatology*, W. Kirchofer, A. Ohmura, and W. Wanner, Eds., Zurcher Schriften, 19–29.

Pielke, R. A., Sr., 2002: *Mesoscale Meteorological Modeling.* 2nd ed. Academic Press, 676 pp.

——, G. Marland, R. A. Betts, T. N. Chase, J. L. Eastman, J. O. Niles, D. Niyogi, and S. Running, 2002: The influence of land-use change and landscape dynamics on the climate system: Relevance to climate-change policy beyond the radiative effect of greenhouse gases. *Philos. Trans. Roy. Soc. London*, **A360**, 1705–1717, doi:10.1098/rsta.2002.1027.

Potter, C., 2014: Understanding climate change on the California coast: Accounting for extreme daily events among long-term trends. *Climate*, **2**, 18–27, doi:10.3390/cli2010018.

Reynolds, R. W., 1988: A real-time global sea surface temperature analysis. *J. Climate*, **1**, 75–86, doi:10.1175/1520-0442(1988)001<0075:ARTGSS>2.0.CO;2.

Rousseeuw, P. J., 1987: Silhouettes: A graphical aid to the interpretation and validation of cluster analysis. *J. Comput. Appl. Math.*, **20**, 53–65, doi:10.1016/0377-0427(87)90125-7.

Sailor, D., 1995: Simulated urban climate response to modifications in surface albedo and vegetative cover. *J. Appl. Meteor.*, **34**, 1694–1704, doi:10.1175/1520-0450-34.7.1694.

Schmid, H. P., and T. R. Oke, 1992: Scaling North American urban climates by lines, lanes and rows. *Geographical Snapshots of North America*, D. G. Janelle, Ed., Guildford Press, 442 pp.

Shepherd, J. M., W. M. Carter, M. Manyin, D. Messen, and S. Burian, 2010: The impact of urbanization on current and future coastal convection: A case study for Houston. *Environ. Plann.*, **37B**, 284–304, doi:10.1068/b34102t.

Skamarock, W. C., and Coauthors, 2008: A description of the Advanced Research WRF version 3. NCAR Tech. Note NCAR/TN-475+STR, 113 pp., doi:10.5065/D68S4MVH.

Snyder, M. A., L. C. Sloan, N. S. Diffenbaugh, and J. L. Bell, 2003: Future climate change and upwelling in the California Current. *Geophys. Res. Lett.*, **30**, 1823, doi:10.1029/2003GL017647.

Taha, H., 1994: Meteorological and photochemical simulations of the south coast air basin. Analysis of Energy Efficiency of Air Quality in the South Coast Air Basin—Phase II, Lawrence Berkeley National Laboratory Rep. LBL-35728, 161–218.

——, H. Akbari, A. Rosenfeld, and J. Huang, 1988: Residential cooling loads and the urban heat island—The effects of albedo. *Build. Environ.*, **23**, 271–283, doi:10.1016/0360-1323(88)90033-9.

U.S. Census Bureau, 2010: Vintage 2010: National tables: Annual population estimate. U.S. Census Bureau, accessed 20 July 2014. [Available online at http://www.census.gov/popest/data/historical/2000s/vintage_2009/index.html.]

Vermote, E., D. Tanré, J. L. Deuzé, M. Herman, and J. J. Morcrette, 1994: Second simulation of the satellite signal in the solar spectrum (6S). 6S User's Guide Version 1, NASA-GSFC, 134 pages.

Walters, J. T., R. T. McNider, X. Shi, W. B Norris, and J. R. Christy, 2007: Positive surface temperature feedback in the stable nocturnal boundary layer. *Geophys. Res. Lett.*, **34**, L12709, doi:10.1029/2007GL029505.

Yoshikado, H., 1992: Numerical study of the daytime urban effect and its interaction with the sea breeze. *J. Appl. Meteor.*, **31**, 1146–1164, doi:10.1175/1520-0450(1992)031<1146:NSOTDU>2.0.CO;2.

——, 1994: Interaction of the sea breeze and urban heat islands of different sizes and locations. *J. Meteor. Soc. Japan*, **72**, 139–142.

Zhang, H., A. Henderson-Sellers, and K. McGuffie, 1997: Impacts of tropical deforestation. Part II: The role of large-scale dynamics. *J. Climate*, **10**, 2498–2521, doi:10.1175/1520-0442(1996)009<2498:IOTDPI>2.0.CO;2.